Oxygen production by solar vapor-phase pyrolysis of lunar regolith simulant

Rok Šeško, Kim Lamboley, Thierry Cutard, Laura Grill, Philipp Reiss, Aidan Cowley

Acta Astronautica 224 (2024) 215–225

Contents lists available at ScienceDirect

Acta Astronautica

journal homepage: www.elsevier.com/locate/actaastro

Research paper

Oxygen production by solar vapor-phase pyrolysis of lunar regolith simulant

Rok Šeško [a,b,*], Kim Lamboley [b,c], Thierry Cutard [d], Laura Grill [a], Philipp Reiss [a], Aidan Cowley [b]

[a] Technical University of Munich, Lise-Meitner-Str. 9, Ottobrunn, 85521, Germany
[b] European Space Agency, European Astronaut Centre, Linder Höhe, Cologne, 51147, Germany
[c] Kungliga Tekniska Högskolan, KTH School of Engineering Sciences, Brinellvägen 8, Stockholm, 114 28, Sweden
[d] Institut Clément Ader (ICA), Université de Toulouse, CNRS, IMT Mines Albi, INSA, ISAE-SUPAERO, UPS, Campus Jarlard, Albi, F-81013, France

ARTICLE INFO

Keywords:
Lunar regolith
Oxygen extraction
Pyrolysis
Solar energy
Thermochemical modeling

ABSTRACT

The oxide-rich lunar surface regolith can be used to extract the oxygen needed for the future of lunar exploration efforts as a consumable for life-support systems and spacecraft propulsion. Various techniques for the extraction of oxygen have been developed already, with solar vapor-phase pyrolysis shown to be a promising yet understudied approach. In contrast to other techniques, it requires only locally available resources, such as unbeneficiated regolith, sunlight, and vacuum in order to liberate oxygen and oxygen-bearing molecules. This study presents experimental work conducted in a purpose-built solar-vacuum furnace showing the evaporation of sodium and iron from a regolith simulant sample and their deposition on the crucible surface. This is matched by the thermochemical equilibrium modeling done in FactSage, which analyzes the process at varying pressures down to ultra-high vacuum. It highlights the need for precise temperature and pressure control, as well as the impact of regolith composition on oxygen dissociation for an efficient extraction of molecular oxygen.

1. Introduction

The lunar surface environment can yield a wealth of resources suitable for lunar surface exploration and missions eventually progressing beyond lunar orbit. In the context of human spaceflight, the focus of ISRU (In-Situ Resource Utilization) has been on extracting oxygen, a valuable product for life-support systems and an important consumable for spacecraft propulsion. Multiple oxygen extraction techniques have been studied and developed to different levels of technological readiness [1–3]. The focus of this study is solar vapor-phase pyrolysis of lunar regolith simulant, which remains a promising if understudied approach, with a lower technology readiness level compared to other techniques that have been developed in recent years. In principle, solar pyrolysis has the potential of using only locally available resources, namely lunar environment vacuum, regolith, and sunlight for thermal reduction of regolith constituents without requiring any consumables or significant amounts of electricity. This study aims to show that solar vacuum pyrolysis could be further developed as a viable oxygen extraction technique, as well as being a tool for vacuum distillation of other elements present in the regolith.

2. State of the art

Pyrolysis requires regolith of any composition and a heat source, which can be provided by electric resistive, inductive, or microwave heating. In contrast to electric heating, which requires high-power electricity generation on the Moon, regolith can also be heated directly by concentrated sunlight. Such a reactor would likely require less infrastructure [4–7] while being able to reach temperatures on the order of 2000 K [8,9]. These temperatures are sufficient for full or partial reduction of regolith in a rough vacuum. The dissociation temperature, where regolith oxides are reduced is known to fall with lower pressures [10]. These lower process temperatures in the high vacuum range present on the lunar surface should be beneficial for lower energy consumption and thermal loads on a pyrolysis reactor.

Shaw et al. [11] proposed pyrolysis of regolith at even lower pressures and temperatures, predicting thermal decomposition of regolith in the range of 1100 K at pressures of 10^{-12} mbar. Shaw [12] also demonstrated thermal decomposition by sublimation of Na and K from the LMS-1 lunar regolith simulant [13]. The process at these conditions lies in the sublimation regime, where evaporation and dissociation of oxides occur from solid regolith, instead of a molten state. Pyrolysis in this regime is too slow for industrial applications [11,12]. High throughput pyrolysis reactors should benefit from higher reaction kinetics at higher pressures and temperatures (>1300 °C) [11,12].

Experimental studies of solar pyrolysis have previously been performed at higher pressures and above the liquidus temperature to

* Corresponding author at: Technical University of Munich, Lise-Meitner-Str. 9, Ottobrunn, 85521, Germany.
E-mail addresses: rok.sesko@tum.de (R. Šeško), aidan.cowley@esa.int (A. Cowley).

https://doi.org/10.1016/j.actaastro.2024.08.009
Received 30 January 2024; Received in revised form 12 July 2024; Accepted 8 August 2024
Available online 17 August 2024

target the higher reaction kinetics in that region. Proof of principle work was performed by Sauerborn [14] at the German Aerospace Center's (DLR) solar furnace [15], heating the regolith simulant JSC-1A [16] and simple oxides to temperatures of 1300 °C to 1500 °C at pressures of 10^{-5} mbar to 10^{-4} mbar. These activities have qualitatively demonstrated oxide dissociation and oxygen production. A second study was performed by Matchett [10] using a smaller Fresnel lens solar concentrator. It demonstrated the reduction of several simple oxides and Minnesota lunar simulant MLS-1 [17] with experiments performed between 10^{-4} mbar and 1 mbar and temperatures of 900 °C to 1900 °C.

These past studies present proof that the underlying concept of solar vapor-phase pyrolysis is feasible, but leave considerable pressure and temperature ranges to be characterized in terms of process behavior and, ultimately, engineering performance.

3. Methodology

Dissociation conditions throughout a more extensive pressure range of 10^{-8} mbar to 10^{3} mbar are studied in this work through thermochemical equilibrium modeling. Initial experimental work on a dedicated solar vacuum furnace is presented along with experimental results in the pressure range between 10^{-5} mbar and 10^{-2} mbar.

3.1. Thermochemical modeling

Understanding the temperature–pressure dependence of pyrolysis and its products is vital for its study, development, and optimization. To calculate the amounts of oxygen produced from regolith at different pyrolysis conditions, thermochemical equilibrium calculations were performed at discrete constant temperature and constant pressure conditions. A similar approach to Shaw et al. [11] was taken by using Gibbs free energy minimization computation in the FactSage 8.1 software package [18].

Computation of thermochemical equilibria in FactSage relies on extensive databases of thermodynamic data for multicomponent systems. Properties of complex multicomponent systems are computed in FactSage by evaluation of several two or three-component systems through Gibbs free energy minimization [18–20].

The calculations presented in this work are in an assumed steady-state condition and do not take the reaction kinetics of pyrolysis into account, which are considerably slow relative to high-temperature reactions, as noted previously in literature [6,11,12].

The following assumptions were made for the thermochemical calculations:

- The system is assumed to be at chemical equilibrium. All reactions with slow reaction kinetics have been completed.
- Material composition is homogeneous and has no local differences. All compounds, atoms, or molecules can interact with each other and achieve the lowest possible energy state.
- The regolith sample does not contain any volatile material that would outgas at modeled temperatures or change the thermal or chemical behavior of the sample.
- The heating of the sample is homogeneous.

Even with these boundary constraints and assumptions, these calculations highlight the pressure and temperature regions, which have the highest potential for oxygen extraction.

3.1.1. Modeled regolith compositions

Three regolith compositions and one regolith simulant composition (Table 1) were used in thermochemical simulations. They were selected to cover the most typical lunar regolith compositions. The Luna sample 24999, the Apollo sample 64501, and the Apollo sample 70051 were selected as the regolith compositions. According to Papike et al. [21], samples 24999 and 64501 are "pure" representations of a Mare and Highland regolith composition, respectively. These two samples have also been used in the previous thermochemical simulations by Shaw et al. [11]. The Apollo sample 70051 [22] was chosen as a high-titanium regolith sample to compare its behavior to the low-titanium Mare sample 24999. It is not the highest titanium-content sample, but it is an overall interesting sample for ISRU investigations, as proposed by Hill et al. [22] because it is a mixture of soils from a large area of the Apollo 17 landing site. The final modeled composition is the EAC-1A lunar regolith simulant [23] with chemical composition data from Alvarez [24].

Table 1
Regolith and regolith simulant geochemical compositions in % by weight used for thermochemical simulations. Oxide fractions are taken from [21] for 24999 and 64501, [22] for 70051, and [24] for EAC-1A.

Oxide	24999, Mare	64501, Highland	70051, High-Ti Mare	EAC-1
SiO_2	44.61	45.42	43.22	44.41
FeO	20.83	4.49	12.70	0.00
MgO	10.97	4.39	10.55	12.09
CaO	10.87	16.77	11.78	10.98
Al_2O_3	10.77	27.85	16.08	12.80
TiO_2	0.99	0.45	5.21	2.44
Cr_2O_3	0.42	0.08	0.00	0.00
MnO	0.28	0.06	0.15	0.20
Na_2O	0.23	0.40	0.25	2.95
K_2O	0.02	0.09	0.07	1.32
Fe_2O_3	0.00	0.00	0.00	12.20
P_2O_5	0.00	0.00	0.00	0.61
Total	99.99	100.00	100.01	100.00

3.1.2. Range of modeled reactor conditions

The results given by FactSage are discrete equilibrium points on a grid of pressures from 10^{-8} mbar to 10^{3} mbar and temperatures from 298 K to 3773 K. Upper and lower pressure bounds were chosen between Earth's atmospheric pressure of 10^{3} mbar and 10^{-8} mbar which is one order of magnitude less than the proposed pressure of 10^{-7} mbar for lunar operations of a vapor-phase pyrolysis reactor by Cardiff et al. [25] and two orders of magnitude less than the empirical experiments presented in this work. This covers the range of interest for investigating pyrolysis behavior in vaporization and sublimation ranges, as well as the lowest initial pressures of 10^{-8} mbar to 10^{-7} mbar reached in the presented experimental reactor before solar illumination. The upper-temperature limit of 3773 K was chosen to capture the complete vapor phase transition of all modeled pressures with margin. At this temperature only the highest modeled pressure of 10^{3} mbar does not reach full vaporization but only a gas fraction of 99%.

3.2. Experiment

To demonstrate the process and produce data for comparison with the model results, vacuum pyrolysis experiments using EAC-1A regolith simulant [23] were performed in a purpose-built small-scale high-vacuum solar furnace [26].

3.2.1. Experimental setup

The experimental setup (see Fig. 1) consists of a vacuum chamber and an optical system, which is used for the concentration of sunlight into the vacuum chamber to heat the regolith sample. The optical system consists of two mirrors: a pivotable heliostat used to redirect the solar rays horizontally and a fixed mirror at 45° that redirects the horizontal rays along the vertical axis and into a Fresnel lens. The optical system can rotate along the vertical axis to follow the azimuth angle of the Sun. The horizontally positioned Fresnel lens focuses the light through a quartz glass window (CF DN 100 window with a 98.6 mm aperture diameter) and onto the surface of the regolith sample in an alumina crucible inside the vacuum chamber (see Fig. 2). While the sunlight is heating the sample, the temperature of the regolith

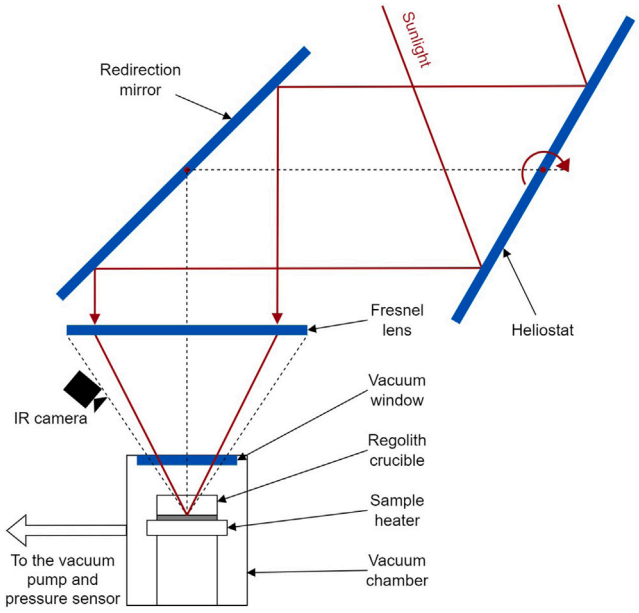

Fig. 1. Schematic of the experimental setup.

surface is measured using an IR camera looking through the quartz glass window. The pressure of the vacuum chamber is also monitored using pressure sensors mounted on the chamber.

The pressure was monitored at the exit of the vacuum chamber (see schematic in Fig. 1). The temperature measurements were performed by an Optris PI 1M infrared camera placed on a tripod on the side of the Fresnel lens and looking down in the chamber through the solar window. This infrared image of the crucible was analyzed through the Optris PIX Connect software and the maximum temperature with an emissivity of 0.98 was extracted and used as a reference temperature for the process.

3.2.2. Experimental procedure

A solar experiment campaign lasted for two full days. The first day allowed the system to reach ultra-high vacuum (UHV) and the second day was used for exposure of the sample to the concentrated sunlight.

During an experiment, a 10 g EAC-1A simulant sample was placed in an alumina ceramic crucible and then moved inside the vacuum chamber. The chamber top was then sealed with a copper gasket and the quartz glass viewport. The vacuum pumps were turned on to decrease the pressure down to approximately 10^{-5} mbar. Then, all the vacuum channels (pipes and chamber) were heated externally through electrical heating pads to around 180 °C. An internal heater heated the bottom of the crucible directly, allowing the regolith simulant to reach temperatures above 400 °C. This removed potential volatiles accumulated due to adsorption under atmospheric conditions. After 5 h under these conditions, the heaters were turned off while the pump was left running until the next morning.

On the subsequent day, the vacuum pump was temporarily switched off for the transport of the setup outside for the solar exposure. Measured total solar irradiance during the exposure was 860 W m^{-2} to 960 W m^{-2} using a local sensor and 825 W m^{-2} to 903 W m^{-2} based on data from the German Meteorological Service (DWD) [27]. The Fresnel lens' cover was then removed and the solar tracking was performed manually and adjusted every 5 min. The vacuum pumps were operating during the total duration of the exposure.

During the exposure, vacuum pressure measurements oscillated from 10^{-7} mbar to 10^{-2} mbar while the surface temperature of the regolith sample reached in range of 1750 K to 1900 K. These combinations of pressure–temperature can then be used as inputs for the thermochemical modeling in order to predict the species that were pyrolyzed during the experiment.

4. Results and discussion

4.1. Modeling

The results of the thermochemical calculations provide data on solid, liquid, and gas compounds that exist at chosen equilibrium conditions and their thermodynamic properties. This study focuses on the produced oxygen, therefore, the amounts of oxygen and other gases are analyzed in order to obtain an understanding of oxygen evolution from regolith throughout a pressure range of 10^{-8} mbar to 10^{3} mbar and a temperature range of 273 K to 3773 K. Oxygen is produced mainly in the vapor phase transition, which can be observed in Fig. 3. It shows the fractions of solid, liquid, and gas phase at different equilibrium points for the Mare (24999) composition. The other three regolith compositions have also been computed and exhibit qualitatively similar behavior with slight differences in melting and vaporization temperature. All figures in this work show the Mare composition unless noted otherwise. The differences between compositions will be described in the discussion of results.

To discuss regions of interest in the model data, it is valuable to look at the fractions of solid, liquid, and gas components, as shown in Fig. 3. The solid phase exists for the whole pressure range below 1350 K except for pressures below 10^{-5} mbar, where vaporization or sublimation begins below 1300 K. Vaporization is used in the following text when referring to boiling and evaporation or sublimation.

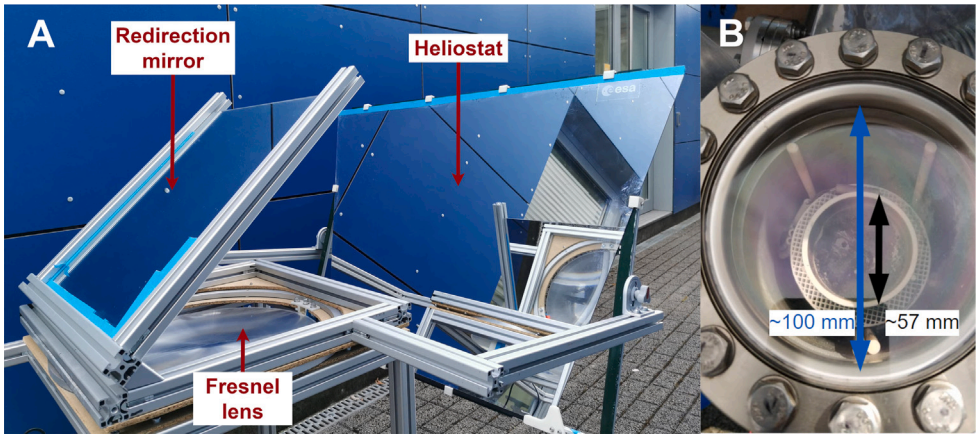

Fig. 2. Optical system of two mirrors and a Fresnel lens on the left; window of the vacuum chamber on the right.

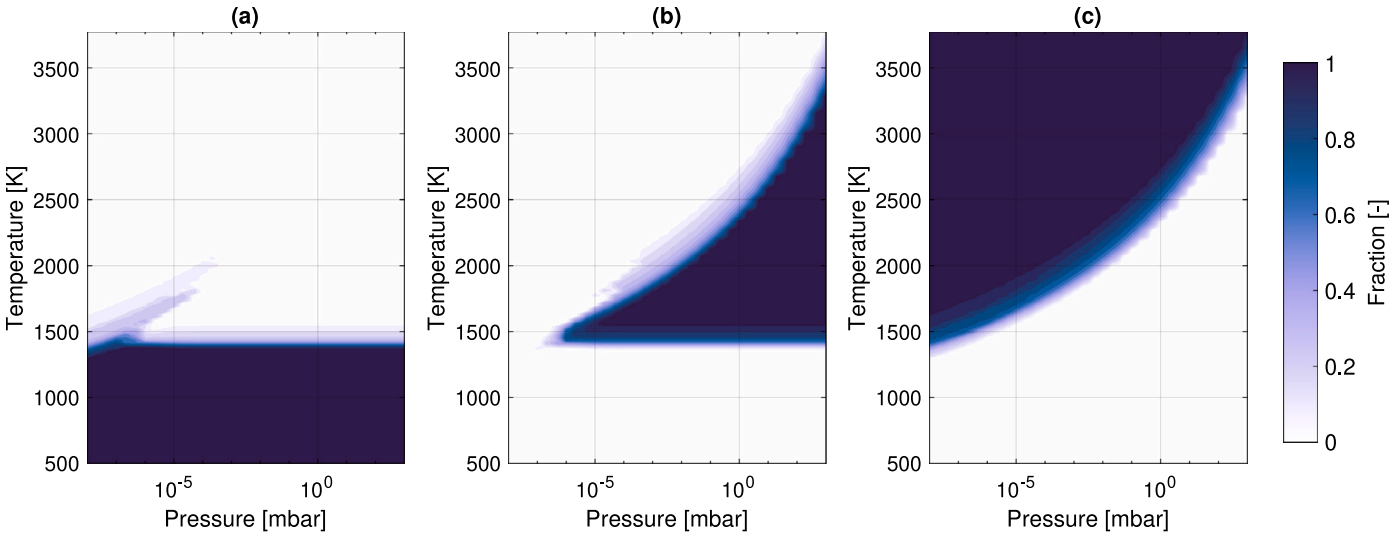

Fig. 3. Fraction of solid (a), liquid (b), and gas (c) throughout the parameter space of FactSage calculations for the Mare (24999) composition.

Above this pressure threshold of approximately 10^{-5} mbar and until the top of the pressure range, a melting phase transition can be observed between 1350 K and 1530 K. Subsequently, a liquid state (Fig. 3b) can then be observed until we reach the large pressure-dependent vaporization curve boundary spanning approximately 1500 K to 3500 K. For instance, the onset of vaporization is seen at approximately 1800 K for the pressure of 10^{-3} mbar and at 2100 K at a pressure of 10^{-1} mbar.

The vaporization temperature decreases as pressure decreases until the vaporization regime crosses the melting temperature range between 1400 K and 1500 K. Below that intersection on the pressure axis, the sublimation of solid material directly to gas can be observed due to the lack of a liquid phase between solid and gaseous phase fractions. Pyrolysis in this sublimation region was proposed previously by Shaw et al. [28]. It might provide easier post-reduction handling of solid particles instead of the solidified melts. Additionally, the lower temperature requirements for the pyrolysis reactor would be advantageous. These calculations indeed show pyrolysis occurring at relatively low temperatures just below the melting range for pressures below 10^{-5} mbar. Due to the abstraction level of this modeled regolith state, actual sublimation in a real reactor cannot be assumed. Shaw [12,29] noted that the FactSage calculation results for vapor pressures of sublimated material vary significantly from the measured data. Above the vaporization temperature range, only the gas phase can still be observed in Fig. 3c.

4.1.1. Gas evolution

Different oxides present in regolith dissociate at distinct temperatures, resulting in the production of specific gasses at particular temperatures during the vapor transition. To gain insight into the gas evolution and its dependency on temperature and pressure, the composition of produced gas is presented in Fig. 4. Fig. 4a shows gas evolution as a mass fraction of initial bulk regolith, and Fig. 4c shows the gas evolution as a mass fraction of total produced gas at 10^{-5} mbar for each temperature.

Similar gas evolution can be observed at other pressures with a shifted temperature range, where the shift follows the vapor phase transition as shown in Fig. 3b. Figs. 4b and 4d show the gas evolution at 1 mbar which is qualitatively similar to the evolution at 10^{-5} mbar, only shifted approximately 800 K higher. Notably, sodium and iron represent a larger fraction of the gas phase in the 10^{-5} mbar case at 1373 K and 1563 K, respectively. The evaporation of sodium and potassium occurs at slightly higher temperatures, closer to those of iron and silicon in the latter case. Therefore, it is not clearly visible in Fig. 4d since they represent a smaller fraction of gas in comparison to other species with more initial mass, e.g. Fe, Si, Mg, and O. Some minor gas species (e.g. TiO_2 and CrO) were left out of the figure for clarity since they do not contribute significantly to the gas quantity.

The oxides contained in regolith dissociate in the following order: Na_2O, K_2O, FeO, SiO_2, MgO, CaO, CrO_2, TiO_2, and Al_2O_3. This order aligns with results from the literature [10,28] and with results obtained with the experimental setup. High amounts of Na and K as well as traces of Fe and Si are observed on the crucible surface (via EDX, Fig. 15), which are precisely the species expected to appear towards the lower part of pyrolysis temperatures.

4.1.2. Oxygen yield

Oxygen yield is the critical parameter for the development of the process, defined as the mass of the product divided by the mass of raw regolith feedstock [30]. It is important to define the yield for molecular oxygen O_2 and atomic oxygen production separately instead of a combined O_2 and O production since atomic oxygen can recombine into O_2 or aggressively react with reactor hardware and other suboxide species, which can be detrimental to the reactor or the final oxygen yield [10]. Therefore, O_2 and O yields are studied separately here. How these values are used further needs to be defined based on the gas processing steps after pyrolysis and a real reactor design, which are not a part of this work. Molecular oxygen (O_2) yield is shown in Fig. 5a. The highest values for each discrete pressure are called peak yields in the following sections. Peak yield drops off towards the higher pressures where the peak yield only reaches up to 10% for a given temperature.

Atomic oxygen (O) yield, shown in Fig. 5b, increases from nearly 0% at the temperatures where O_2 yield peaks to values above 40%. At full vaporization and dissociation of oxides, all of the oxygen present in the initial regolith is in an atomic state. The transition from 0% to 25% O yield roughly follows the vapor phase transition. There is a second transition visible from approximately 25% to 40%. This can be attributed to the dissociation of gaseous SiO, which is the last suboxide to dissociate to Si and O. This can be seen in Fig. 4a, which shows the composition of the gas phase for different temperatures at 10^{-5} mbar. Above approximately 2700 K a decrease in the weight of SiO and an increase in Si and O can be seen. This dissociation of suboxide species that occurs in the gaseous state is likely not relevant for this process because the gas in a real reactor is not heated at a rate that would increase its temperature significantly above the vaporization temperature of the melt.

Three derived yield parameters are recognized as relevant for the optimization of the process with regard to pressure and temperature

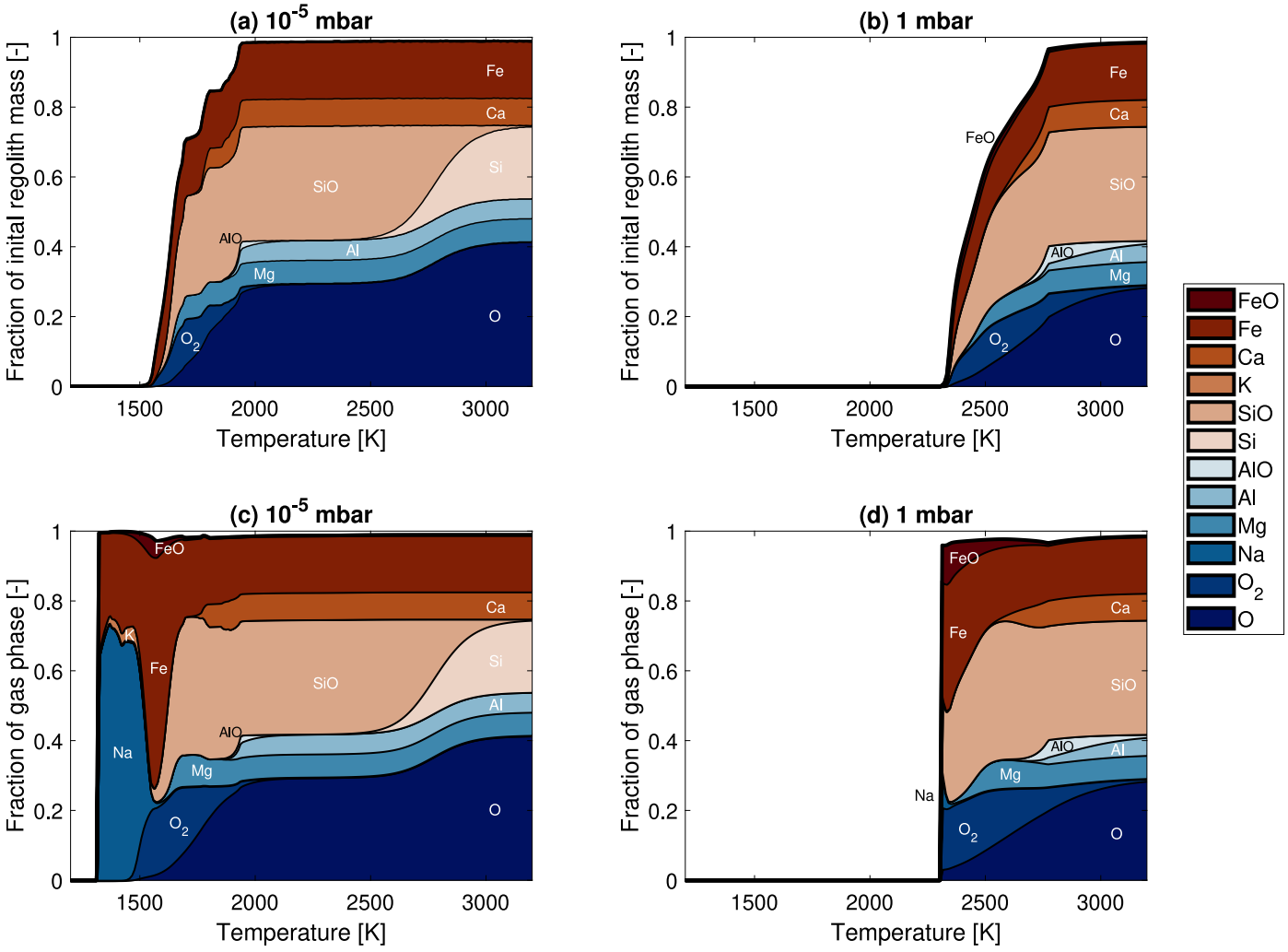

Fig. 4. Mare (24999) regolith dissociation: gaseous species mass as a fraction of initial regolith mass at 10^{-5} mbar (a) and at 1 mbar (b); gaseous species mass as a fraction of total gas mass at 10^{-5} mbar (c) and at 1 mbar (d). Major species visible in each plot are labeled for improved readability in addition to the legend. Minor species with a maximum fraction below 2.5% in all of the plots are omitted from all for clarity.

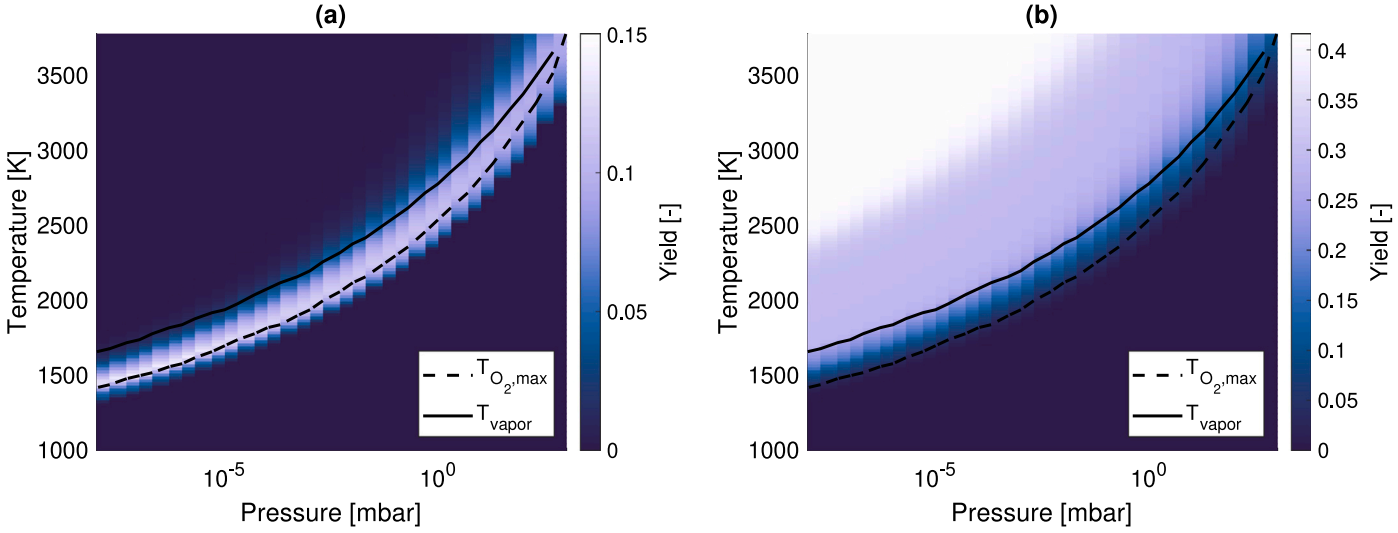

Fig. 5. Oxygen yield from FactSage calculations for the Mare 24999 composition: (a) molecular oxygen, (b) atomic oxygen. Lines mark the full vaporization temperature (T_{vapor}) and the temperature of the maximum O_2 yield ($T_{O_2,max}$).

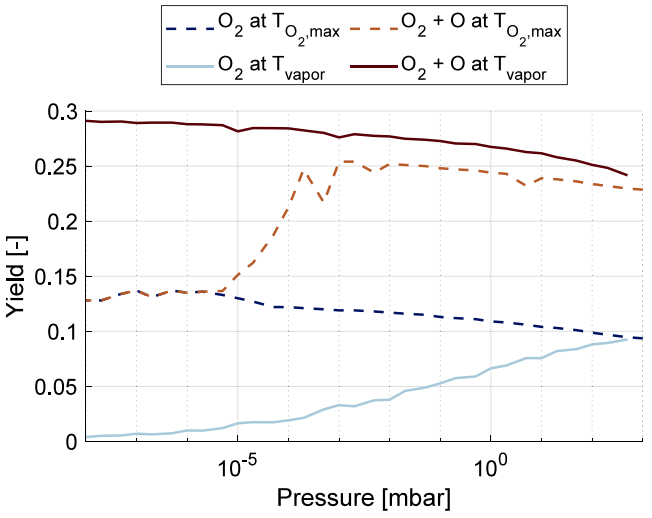

Fig. 6. Molecular, atomic, and combined oxygen yield at the full vaporization temperature (T_{vapor}) and at the temperature of the maximum O_2 yield ($T_{O_2,max}$).

conditions. The first and most conservative is the peak O_2 yield for each pressure. Additionally, the peak atomic oxygen (O) yield for each pressure can also be considered on its own or combined with molecular oxygen as the combined peak oxygen (O_2 + O) yield. Both these parameters can be analyzed at two relevant temperature conditions for each pressure. The first is the temperature where the peak O_2 yield occurs ($T_{O_2,max}$). The second is the temperature where 99% of the melted material is in a gaseous state (T_{vapor}).

A comparison of the described yield values of O and O_2 is shown in Fig. 6 for all of the modeled pressures. The molecular oxygen yield can be considered the conservative yield estimate, while the combined peak oxygen is the best-case estimate, which depends on the pathways for the utilization of atomic oxygen. If further processing of atomic oxygen is possible, pressures above 10^{-3} mbar show higher yield at lower temperatures. The combined oxygen yield at $T_{O_2,max}$ nearly reaches the values of the combined yield at T_{vapor}. The lower temperature might be attractive due to the lower temperature and power requirements for the reactor. All yield data at T_{vapor} in Figs. 6 and 7 is shown only up to 10^2 mbar due to incomplete vaporization of regolith in calculations at the highest pressure data point of 10^3 mbar.

4.1.3. Comparison of regolith compositions

Another consideration in this study is the difference in oxygen yield across the four regolith compositions analyzed. Fig. 7 shows the yields for the combined oxygen yield at T_{vapor} and $T_{O_2,max}$, and the peak molecular oxygen yield for each pressure (O_2 yield at $T_{O_2,max}$). In the case that both molecular and atomic oxygen are usable for further processing steps, the highland regolith compositions show the most potential at the vapor temperature (Fig. 7a), while Low-Titanium Mare (24999) and High-Titanium Mare (70051) compositions show lower yields. On the other hand, Mare compositions show better yield across the analyzed pressure range in the case where only molecular oxygen is of use for further processing (Fig. 7c). Low-Titanium Mare is, in this case, superior to the High-Ti Mare since the Ti-bearing minerals dissociate only at higher temperatures, while the oxides with lower pyrolysis temperatures FeO, SiO_2, and MgO are responsible for molecular oxygen production in the low-temperature range.

4.1.4. Oxygen production in comparison to literature

The thermochemical modeling of the different gas species at different temperatures is consistent with a previously developed model by Shaw et al. [28] with a comparison between the evolved gas

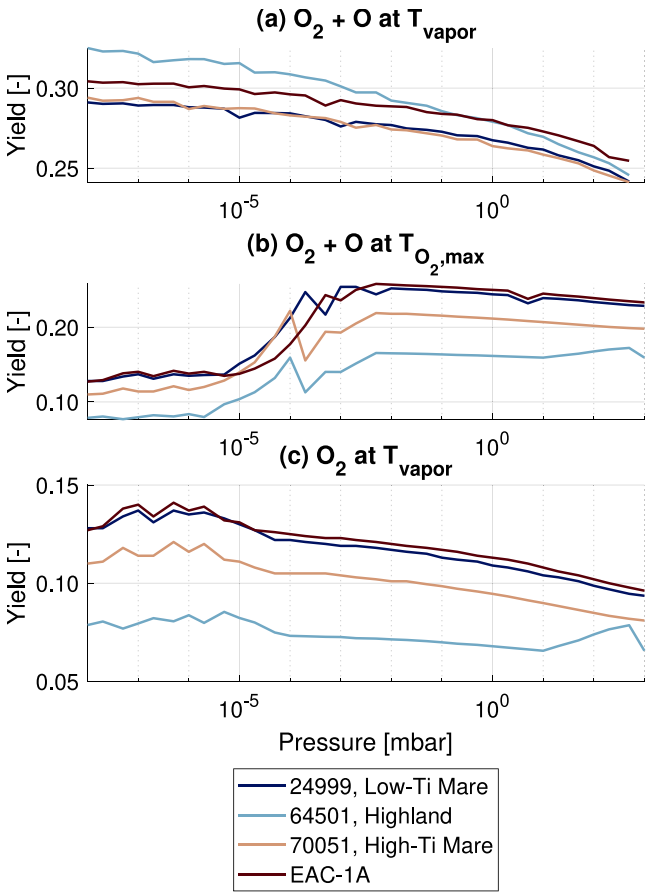

Fig. 7. Oxygen yields for four different regolith compositions (Mare 24999; Highland 64501, High-Ti Mare 70051, EAC-1A): (a) combined O_2 and O yield at full vaporization temperature T_{vapor}; (b) combined O_2 and O yield at full vaporization temperature T_{vapor}; (b) O_2 yield for temperature $T_{O_2,max}$ where O_2 yield is maximized for each pressure.

compositions made in Šeško [26]. The dissociation behavior can also be compared with the calculations done by Matchett [10]. The order of dissociation of the species is very similar, with one slight difference. MgO is shown to dissociate before SiO_2, although the dissociation ranges are heavily overlapping in both studies. This can potentially stem from the use of a different regolith composition (average composition of the Apollo 15 samples) for the calculation in Matchett [10].

A comparison of equilibrium oxygen yields with values from literature is given in Table 2 . Pyrolysis can be divided into two major categories: low-temperature pyrolysis (2000–2200 K), and high-temperature pyrolysis (>2500 K), according to Senior [6]. In the low-temperature range, O_2 is produced mostly from FeO, SiO_2, and MgO, which is consistent with the stated pyrolysis behavior in Senior [6] and Matchett [10]. Maximum O_2 yields given in Senior [6] for the low-temperature range are given as 16% and 20% for highland and mare soils, respectively. Maximum yields calculated in this work lay between 9% and 14% for highland and mare soils, respectively. These yields are approximately 30% lower compared to the values stated by Senior [6] but similar to the values from Matchett [10].

Based on this work and Shaw [28], the low-temperature range can additionally be separated into the sublimation regime and the melting regime, where the first is shown to produce the highest peak yields of 14% below 10^{-6} mbar (Fig. 7c). The highest yields in the melting regime reach slightly lower peak yields on the order of 12% to 13% at 10^{-5} mbar.

The high-temperature range during the dissociation of Al, Ti, and Ca oxides primarily shows production of atomic oxygen instead of

Table 2
Equilibrium yield of molecular oxygen reported in the literature in comparison to values calculated in this work.

Source	O_2 yield	Composition	Temp. range	Comments
[4,5]	20%	unclear	~3000 K	O_2 dissociation neglected
[6]	16%	Highland	2000–2200 K	Lower estimate of atomic oxygen
[6]	20%	Mare	2000–2200 K	
[6]	35%	Highland	>2500 K	
[6]	25%	Mare	>2500 K	
[10]	10%–15%	Mare	1800–2100 °C / 1300–1400 °C	Separate yield values for the two ranges not given
This work	9%–14%	Mare, 24999	1500–3700 K	Continuous data throughout the range, including sublimation. Yield decreases with temperature.
This work	7%–9%	Highland, 64501	1500–3700 K	
This work	8%–12%	Mare, 70051	1500–3700 K	

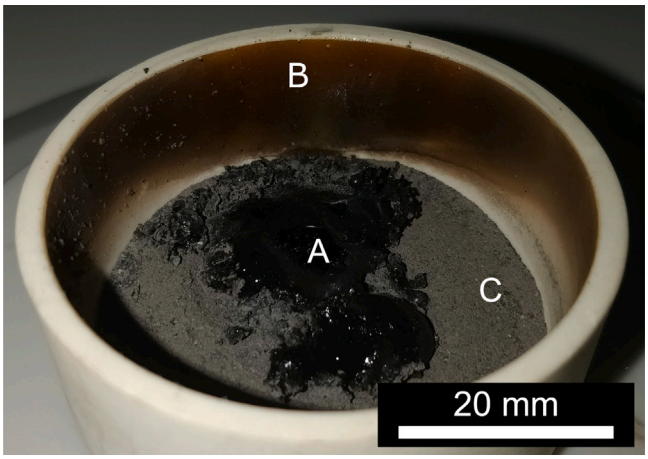

Fig. 8. Crucible with the regolith sample after concentrated solar exposure. Solidified melt is marked (A), condensate on the crucible wall (B), and the rest of the non-melted regolith (C).

molecular oxygen, as shown in Fig. 4a. This contradicts the higher O_2 yield reported for high-temperature pyrolysis in Senior [6], which does not account for oxygen dissociation. Fig. 7c shows a tendency for peak O_2 yields to fall from high yields below 10^{-5} mbar towards higher pressures and higher temperatures (see Table 2).

4.2. Experimental results

The execution of the experimental protocol, results in a processed sample, shown in Fig. 8. The image shows the alumina crucible and the melted regolith simulant (A) on a base of unmelted regolith (C). Additionally, on the inner surface of the crucible, a film of deposited evaporate (B) can be observed. In our analysis, the regolith melt and the crucible walls have been analyzed by scanning electron microscopy (SEM), energy-dispersive X-ray spectroscopy (EDX), and optical microscopy to identify the materials and understand the changes in their material composition and structure arising from the pyrolysis reaction. The melted material and crucible were analyzed using a Nova NanoSEM 450 with an EDAX detector.

SEM imagery of the surface of the melt region can be seen in Fig. 9. The imaged surface is relatively homogeneous and glassy, which is consistent with our previous experience with melting regolith, for example when concentrated microwaves are used to melt the regolith into a glass phase [31]. Notably absent from the pyrolysis surface are crystalline formations near the surface, which are caused by the separation of Mg and Al-rich phases within the melt. Small residual grains of regolith can sporadically be observed on the surface of the first image, likely remnants of unmelted material or moved onto the surface after the experiment from the regolith material below.

A cross-section of the melted sample is shown in Fig. 10, with a number of interesting features. The notable porosity of the sample and the evolution of this porosity from the lower part of the image (where the melt interfaced with the regolith powder bed) towards the top, need to be highlighted. The porosity is most commonly attributed to the formation of gas pockets due to the rapid heating of the regolith simulant material and the release of gas from the pyrolysis reaction, in addition to any adsorbed gasses on the regolith grains. The production of gas is predominantly suspected to occur at this interface region, however, it may also represent an accumulation of trapped gasses during the cooling stages of the melt.

These gas bubbles form at the bottom part of the melt, where the regolith powder is undergoing its conversion to a molten state, and then exfiltrate from the melt. While the true density was not a metric that we are evaluating in this work, we again see similarities to the evolution of the bubbles compared to similar high-temperature microwave processing, wherein regolith that experiences rapid heating and melting leads to a sudden outgassing of volatiles or pyrolysis products, ultimately becoming trapped when the glass cooled [31]. The upper part of the melt, subject to longer solar exposure and forming a more prolonged melt pool, is homogeneous and in a glassy phase state. On the side of the melt and at the bottom interface area, dendrites can be observed of different crystalline forms (Fig. 11A). Similar to what we have observed in microwave melting of regolith, these acicular crystalline structures are caused by the separation of Mg-rich (Fig. 11B) and Al-rich phases (Fig. 11C), likely plagioclase-type minerals.

In addition to the melted regolith on the powder regolith simulant bed, an evaporate deposit was observed in the vicinity of the melted regolith sample (Fig. 8B). It was not immediately apparent if this was only due to a thermal discoloration of the alumina that composes the holding crucible or if a significant amount of material had been deposited via vapor deposition. Fig. 12 shows an SEM image of the material deposited on the crucible surface. We notice two distinct areas of interest: a foamy crystalline formation (top left of the image) and an acicular crystalline formation (bottom and right of the image). EDX analysis of these formations shows that both have high concentrations of K (ranging from 5 to 8 wt%), an element common to regolith simulants (specifically the EAC-1A used in this work). The region with needle-like crystals has a very high concentration of Na (approx. 30 wt%). We also observe the presence of Si ranging from 7 to 20 wt%.

To better characterize the deposit and be able to measure its thickness, the crucible was cut and polished for optical analysis. Fig. 13 shows the crucible cross-section with the deposited material under an optical microscope. The white homogeneous bottom half of the picture is the alumina crucible. The top and black part of the picture is the resin in which the sample was cast for analysis. We observe a 31.3 μm thick white and cloudy deposit on the surface of the crucible. This type of white deposit is present all along the crucible. After some tests taking optical microscope pictures of a crucible surface sample before and after exposure to water and ethanol, it appears that the white crystals of the deposit are soluble in water. As the samples are polished and rinsed with water, some of the deposits could have been removed, explaining the holes visible in the deposit. This would be consistent with the EDX observations that these white crystals are made of Na and K as these elements readily dissolve in water.

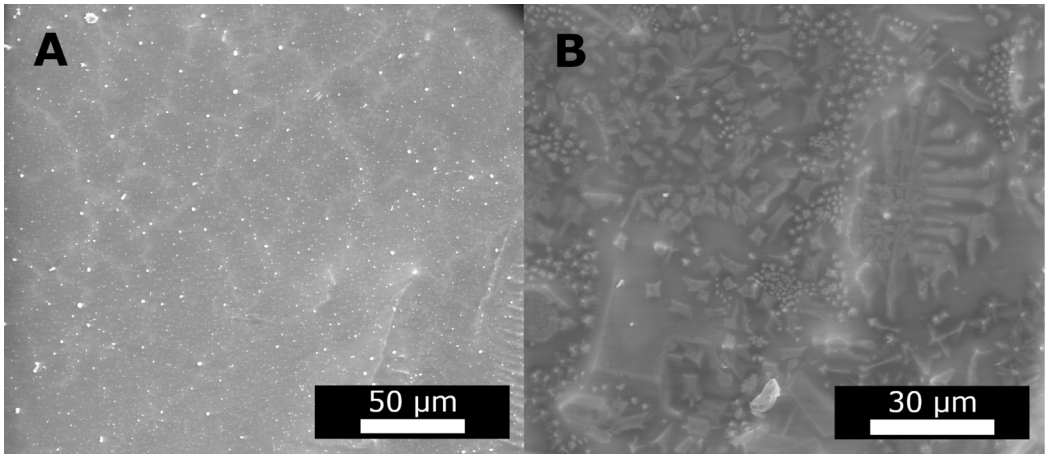

Fig. 9. SEM images of the upper surface of the solidified regolith melt.

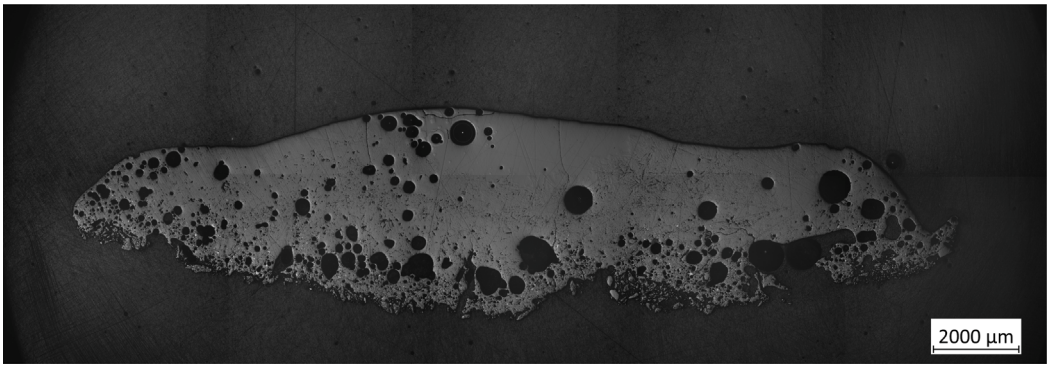

Fig. 10. A cross-sectional view of the regolith melt under an optical microscope.

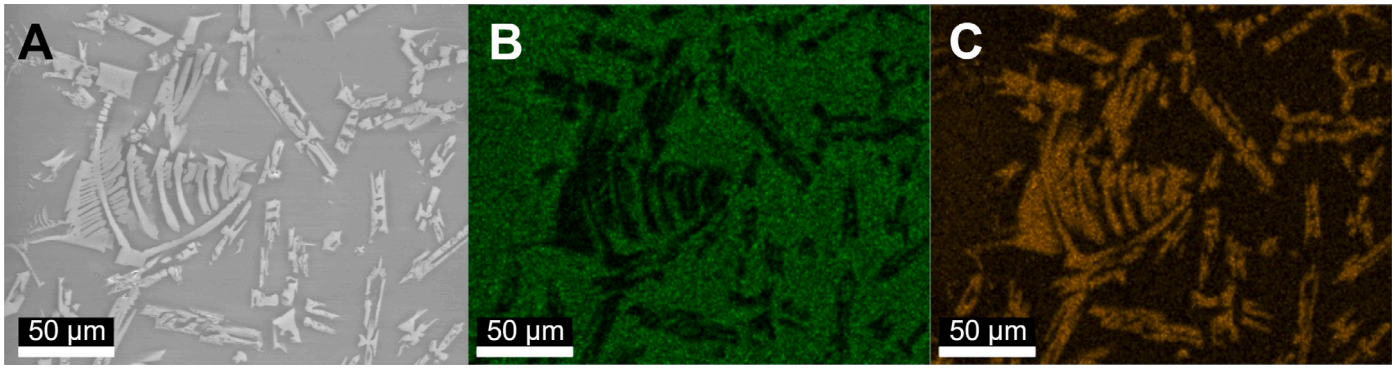

Fig. 11. SEM image (A) of a melt cross-section with the EDX Mg mapping (B) and Al mapping (C).

The evaporated deposit is inhomogeneous in terms of texture and with a non-uniform height; usually around 30 μm of thick white or brown crystal deposits can be seen. Some larger deposits can be seen, which are most likely a mix of melted regolith projectiles that were sputtered on the crucible and the previous Na-rich deposit. In Fig. 14, this type of mountain-like structure was analyzed with an optical microscope (Fig. 14a), SEM (Fig. 14b), and EDX to analyze its composition (Fig. 15). The aim was to get insight into the nature of the orange-brown color in some parts of the white deposits and see what caused the increase in thickness. The elemental mapping in Fig. 15 seems to indicate that the bottom brown layer has a higher concentration of iron than the rest of the deposit. It is consistent with typical iron oxides' red and brown color, even in small concentrations. This could explain why iron was not found in high amounts on the surface EDX analysis if it is present only in the first layer of the deposit and under roughly 30 μm of sodium-rich deposit. A possible explanation of this preferential deposition of iron before sodium is that the conditions for the reduction of iron oxides in the regolith are only present at the beginning of the experiment when pressures are still lower, and the melt pool is still small, thus reaching higher localized temperatures. Throughout the period of solar illumination, pressures tend to rise, the melt pool increases, and thermal contact and corresponding thermal losses from the melt to the surrounding material increase. This lowers the peak temperature in the melt and produces conditions where iron

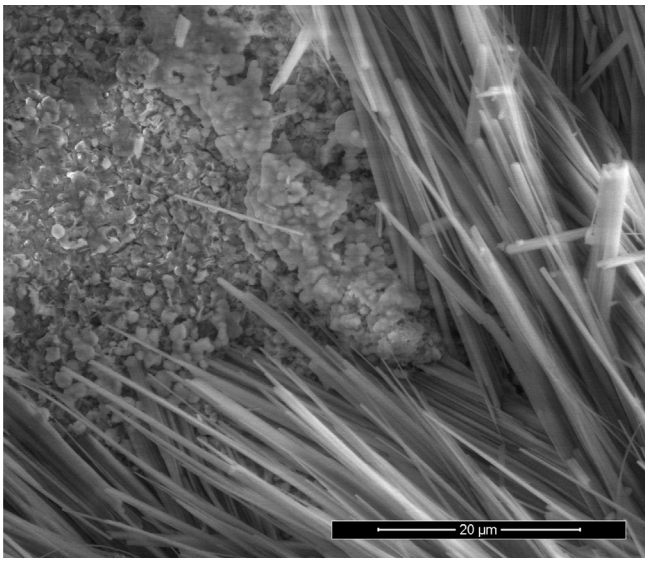

Fig. 12. SEM image of the material deposit on the crucible surface.

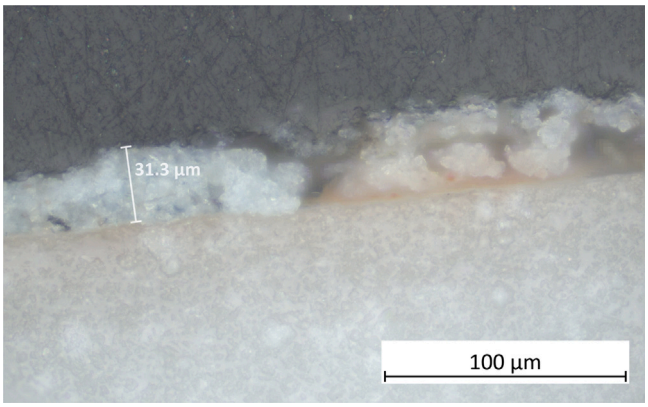

Fig. 13. Optical image of the crucible cross-section and the deposited material.

oxides cannot be pyrolyzed readily, but sodium still can be evaporated. From that point onwards sodium can be observed in the deposit in a larger fraction than iron due to its lower pyrolysis temperature.

4.2.1. Comparison of reactor conditions with modeling results

The preferential deposition of iron before sodium (see Figs. 14 and 15) can be explained by combining the modeling and experimental results. A comparison of the data from FactSage calculations and general experimental conditions is presented in Fig. 16. An envelope of reactor conditions between approximate minimum and maximum temperature and pressure values during a solar exposure is shown to highlight the behavior of gas evolution within it. Important gas species in this condition range are K, Na, and Fe, which begin pyrolyzing towards the bottom right of the drawn envelope. Dashed lines denote the maximum fraction of species mass to total gas mass for each pressure, which exists shortly after pyrolysis begins. Vaporization of these species ends towards the middle of the envelope for K and Na, while Fe vaporization ends in the very upper left corner of the envelope. The end of vaporization for each species is drawn in full lines, which denote the temperature points where gas mass reaches its final and highest value for each of the pressures. Vaporization start, end, and the line of max. O_2 yield are shown for orientation.

These results qualitatively agree with the analysis of condensate produced on the crucible during solar exposure with the preferential deposition of iron and sodium detected by EDX and shown in Fig. 15.

5. Conclusion

Experimental results from a small solar furnace show pyrolysis of regolith in the low-temperature/low-pressure regime, resulting in the production of gas products and deposition of vaporized sodium and iron on the regolith crucible surface.

SEM imaging of the melt region reveals a homogeneous, glassy surface, consistent with previous reports with melted regolith. Gas bubbles form at the base of the melt during the conversion of regolith to a molten state, similar to rapid high-temperature microwave processing. Dendrites of different crystalline forms are observed at the side and bottom interface area, likely representing the separation of Mg-rich and Al-rich phases, such as plagioclase-type minerals, again in good alignment with previous regolith melt behavior [31]. Analysis of the crucible wall deposits shows a preferential deposition profile, whereby iron is initially deposited, followed by sodium and potassium material from the regolith. This behavior is also visible in the modeling of the process in FactSage with sodium, potassium, and iron being the first three oxides to be dissociated in sequence. Considering the evolution of the pressure within the chamber as a function of the process itself, this shows a good correlation between our modeling work and the empirical metrology undertaken.

Modeling results based on equilibrium calculations in FactSage are consistent with previous studies [10,28,29] but cover more pressure and temperature conditions as well as the sublimation range. As expected, the decomposition of low-titanium mare shows higher oxygen yields than high-titanium mare or highland regolith compositions in the low-temperature pyrolysis region. Additionally, the results highlight the importance of choosing the right reactor conditions in order to avoid unnecessary production of atomic oxygen, which decreases the useful molecular oxygen yield. The estimated impact of atomic oxygen production is higher than previously reported [4–6], resulting in lower molecular oxygen yields across the pressure spectrum with equilibrium yields for molecular oxygen ranging from 6.6 to 14.1%.

This research underscores the intricate nature of regolith pyrolysis, particularly concerning the dynamic evolution of the gas phase and the pivotal role of pressure in the overall process, as shown by the modeling work. To leverage this technique effectively for lunar ISRU purposes, there is a pressing need for further exploration and optimization. The promise of this technology, with its inherent simplicity, holds substantial value for various ISRU applications in lunar environments (e.g. oxygen production or vacuum distillation), signifying a compelling avenue for future research and development.

CRediT authorship contribution statement

Rok Šeško: Conceptualization, Investigation, Methodology, Visualization, Writing – original draft, Writing – review & editing, Formal analysis. **Kim Lamboley:** Investigation, Methodology, Writing – original draft. **Thierry Cutard:** Investigation. **Laura Grill:** Supervision, Writing – review & editing. **Philipp Reiss:** Supervision, Writing – review & editing. **Aidan Cowley:** Conceptualization, Project administration, Resources, Supervision, Writing – review & editing.

Declaration of competing interest

The authors declare that they have no known competing financial interests or personal relationships that could have appeared to influence the work reported in this paper.

Acknowledgments

The authors would like to thank Alexandra Adiaconiţei for the invaluable support of the project and Leonardo Facchini for the help with the building of the solar furnace. This work has been supported by the Spaceship initiatives, part of the Exploration Preparation, Research and Technology Team of the European Space Agency. All presented figures use scientific colormaps by Crameri [32].

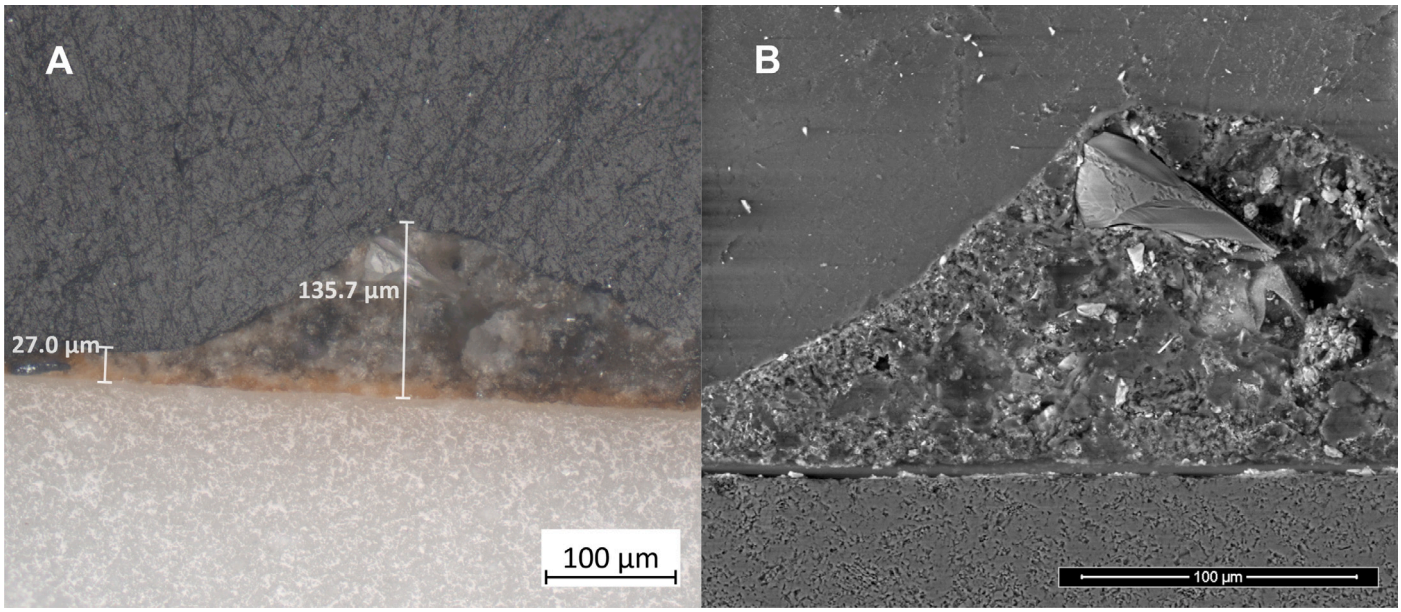

Fig. 14. (a) Optical microscope imagery and (b) SEM imagery of the crucible cross-section.

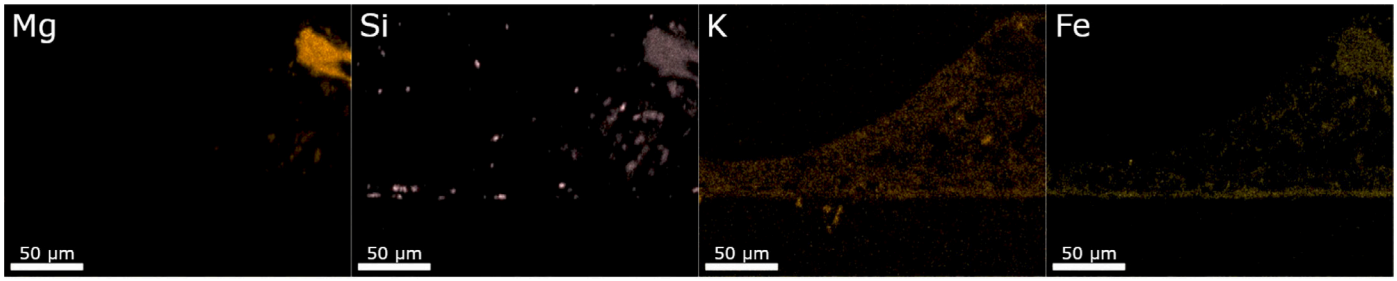

Fig. 15. Mg, Si, K, and Fe EDX maps of the crucible cross-section.

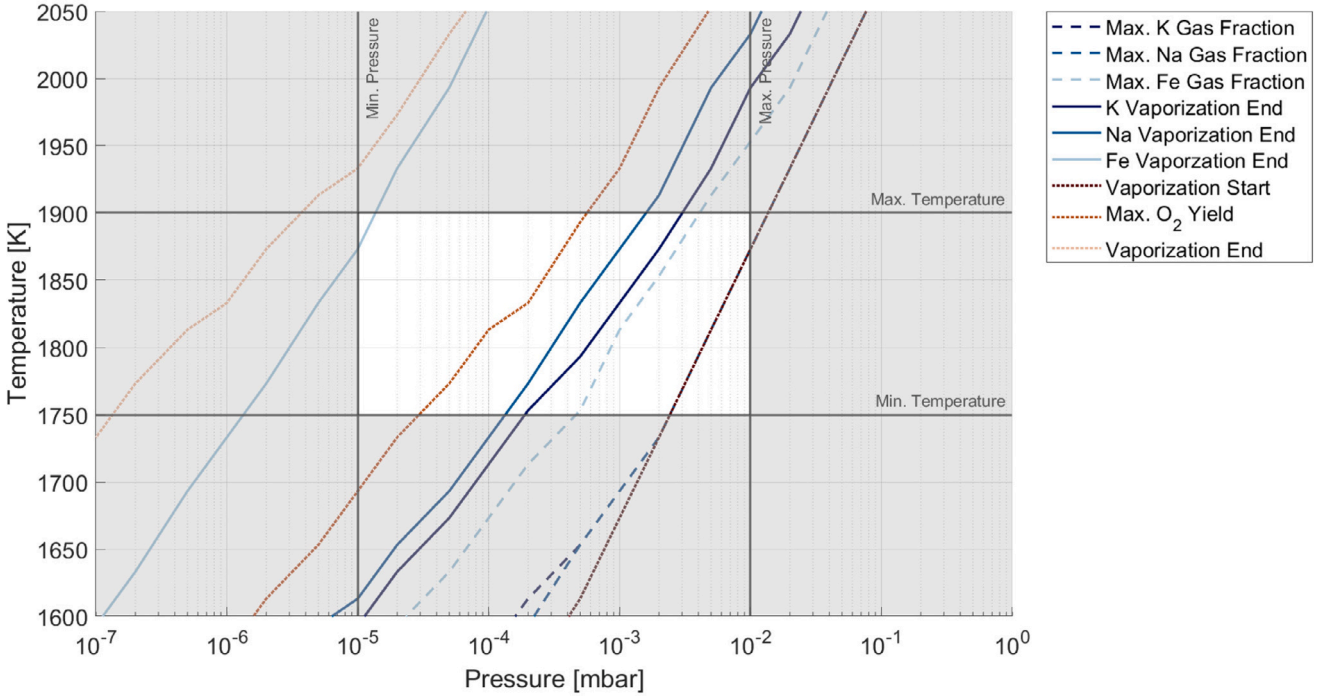

Fig. 16. Comparison of the minimum and maximum pressures and temperatures reached during the solar experiments and the evolution of K, Na, and Fe gas species from pyrolyzed regolith in the FactSage calculations (Mare, 24999).

References

[1] L.A. Taylor, Production of oxygen on the moon: Which processes are best and why, in: AIAA Space Programs and Technologies Conference, 1992, American Institute of Aeronautics and Astronautics Inc, AIAA, 1992, http://dx.doi.org/10.2514/6.1992-1662.

[2] C. Schwandt, J.A. Hamilton, D.J. Fray, I.A. Crawford, Oxygen from lunar regolith, in: V. Badescu (Ed.), first ed., in: Moon: Prospective Energy and Material Resources, vol. 9783642279690, Springer-Verlag Berlin Heidelberg, 2012, pp. 165–187, http://dx.doi.org/10.1007/978-3-642-27969-0_7.

[3] L. Schlüter, A. Cowley, Review of techniques for in-situ oxygen extraction on the moon, Planet. Space Sci. 181 (2020) 104753, http://dx.doi.org/10.1016/J.PSS.2019.104753.

[4] W.H. Steurer, B.A. Nerad, Vapor phase reduction, in: W.F. Caroll (Ed.), Research on the Use of Space Resources, Jet Propulsion Laboratory, NASA, 1983, pp. 1–29, NASA-CR-173213, URL https://ntrs.nasa.gov/api/citations/19840008159/downloads/19840008159.pdf.

[5] W. Steurer, Vapor phase pyrolysis, in: M.F. Mckay, D.S. Mckay, M.B. Duke (Eds.), Space Resources. Volume 3: Materials, NASA. Johnson Space Center, 1992, pp. 210–213, URL https://ntrs.nasa.gov/citations/19930007702.

[6] C. Senior, Lunar oxygen production by pyrolysis, in: AIAA Space Programs and Technologies Conference, American Institute of Aeronautics and Astronautics Inc, AIAA, 1992, http://dx.doi.org/10.2514/6.1992-1663.

[7] Y. Zhang, G. Brooks, A. Rhamdhani, C. Guo, Review on solar thermochemical processing for lunar applications and their heat transfer modeling methods, J. Heat Transfer 143 (2021) http://dx.doi.org/10.1115/1.4052080.

[8] A.R. Clendenen, Concentrated Solar Driven In-situ Resource Utilization for Lunar Exploration (Master's thesis), Georgia Institute of Technology, 2020, URL https://smartech.gatech.edu/handle/1853/65121.

[9] T. Nakamura, A.D.V. Pelt, R.J. Gustafson, L. Clark, Solar thermal power system for oxygen production from lunar regolith, AIP Conf. Proc. 969 (2008) 178, http://dx.doi.org/10.1063/1.2844965.

[10] J. Matchett, Production of Lunar Oxygen Through Vacuum Pyrolysis, Research Report, The George Washington University, 2006, ADA443950, URL https://apps.dtic.mil/sti/citations/ADA443950.

[11] M. Shaw, M. Humbert, G. Brooks, A. Rhamdhani, A. Duffy, M. Pownceby, Mineral processing and metal extraction on the lunar surface - challenges and opportunities, Miner. Process. Extr. Metall. Rev. (2021) http://dx.doi.org/10.1080/08827508.2021.1969390.

[12] M. Shaw, Vacuum Thermal Sublimation for Metal Production from Lunar Regolith (Ph.D. thesis), Swinburne University of Technology, 2023-04, http://dx.doi.org/10.13140/RG.2.2.25263.20646.

[13] M. Isachenkov, S. Chugunov, Z. Landsman, I. Akhatov, A. Metke, A. Tikhonov, I. Shishkovsky, Characterization of novel lunar highland and mare simulants for ISRU research applications, Icarus 376 (2022-04) 114873, http://dx.doi.org/10.1016/j.icarus.2021.114873.

[14] M. Sauerborn, Pyrolyse von Metalloxiden und Silikaten unter Vakuum mit konzentrierter Solarstrahlung (Ph.D. thesis), Rheinischen Friedrich-Wilhelms-Universität Bonn, 2005, URL https://bonndoc.ulb.uni-bonn.de/xmlui/handle/20.500.11811/2298.

[15] A. Neumann, U. Groer, Experimenting with concentrated sunlight using the DLR solar furnace, Sol. Energy 58 (1996) http://dx.doi.org/10.1016/S0038-092X(96)00079-5.

[16] D.S. McKay, J.L. Carter, W.W. Boles, C.C. Allen, J.H. Allton, JSC-1: A new lunar regolith simulant, in: 24th Lunar and Planetary Science Conference, 1993, p. 963, URL https://ui.adsabs.harvard.edu/abs/1993LPI....24..963M.

[17] P.W. Weiblen, K. Gordon, Characteristics of a Simulant for Lunar Surface Materials, in: Second Conference on Lunar Bases and Space Activities of the 21st Century, Vol. 652, 1988, p. 254, URL https://ui.adsabs.harvard.edu/abs/1988LPICo.652..254W.

[18] CRCT, FactSage database documentation, 2022, https://www.crct.polymtl.ca/fact/documentation/. (Accessed 14 August 2022).

[19] C.W. Bale, E. Bélisle, P. Chartrand, S.A. Decterov, G. Eriksson, K. Hack, I.H. Jung, Y.B. Kang, J. Melançon, A.D. Pelton, C. Robelin, S. Petersen, FactSage thermochemical software and databases — recent developments, CALPHAD 33 (2) (2009) 295–311, http://dx.doi.org/10.1016/j.calphad.2008.09.009.

[20] C.W. Bale, E. Bélisle, P. Chartrand, S.A. Decterov, G. Eriksson, A.E. Gheribi, K. Hack, I.H. Jung, Y.B. Kang, J. Melançon, A.D. Pelton, S. Petersen, C. Robelin, J. Sangster, P. Spencer, M.-A. Van Ende, FactSage thermochemical software and databases, 2010–2016, CALPHAD 54 (2016) 35–53, http://dx.doi.org/10.1016/j.calphad.2016.05.002.

[21] J.J. Papike, S.B. Simon, J.C. Laul, The lunar regolith - Chemistry, mineralogy, and petrology, Rev. Geophys. Space Phys. 20 (1982) 761–826, http://dx.doi.org/10.1029/RG020i004p00761.

[22] E. Hill, M.J. Mellin, B. Deane, Y. Liu, L.A. Taylor, Apollo sample 70051 and high- and low-Ti lunar soil simulants MLS-1A and JSC-1A: Implications for future lunar exploration, J. Geophys. Res. Planets 112 (E2) (2007) http://dx.doi.org/10.1029/2006JE002767.

[23] V.S. Engelschiøn, S.R. Eriksson, A. Cowley, M. Fateri, A. Meurisse, U. Kueppers, M. Sperl, EAC-1A: A novel large-volume lunar regolith simulant, Sci. Rep. 10 (1) (2020-03) 5473, http://dx.doi.org/10.1038/S41598-020-62312-4.

[24] M. Alvarez, Study and Characterization of a New Lunar Regolith Simulant: EAC-1A, Internship Report, ESA, 2017.

[25] E.H. Cardiff, B.R. Pomeroy, I.S. Banks, A. Benz, Vacuum pyrolysis and related ISRU techniques, AIP Conf. Proc. 880 (2007) 846, http://dx.doi.org/10.1063/1.2437525.

[26] R. Šeško, Solar-vapor pyrolysis of lunar regolith for oxygen production in high vacuum: an experimental investigation and thermochemical modeling, (Master's thesis), 2022, URL https://mediatum.ub.tum.de/1730482.

[27] D. Wetterdienst, 10-Minütige stationsmessungen der strahlung und sonnenscheindauer für deutschland, Version v23.3, 2023. https://opendata.dwd.de/climate_environment/CDC/observations_germany/climate/10_minutes/solar/. (Accessed 12 September 2023).

[28] M.G. Shaw, G.A. Brooks, M.A. Rhamdhani, A.R. Duffy, M.I. Pownceby, Thermodynamic modelling of ultra-high vacuum thermal decomposition for lunar resource processing, Planet. Space Sci. 204 (2021) 105272, http://dx.doi.org/10.1016/J.PSS.2021.105272.

[29] M.G. Shaw, M.S. Humbert, G.A. Brooks, M.A. Rhamdhani, A.R. Duffy, M.I. Pownceby, Metal and oxide sublimation from Lunar Regolith: A kinetics study, Minerals 13 (1) (2023-01) 79, http://dx.doi.org/10.3390/min13010079.

[30] K. Hadler, D.J.P. Martin, J. Carpenter, J.J. Cilliers, A. Morse, S. Starr, J.N. Rasera, K. Seweryn, P. Reiss, A. Meurisse, A universal framework for Space Resource Utilisation (SRU), Planet. Space Sci. 182 (2020-03) 104811, http://dx.doi.org/10.1016/j.pss.2019.104811.

[31] S. Lim, G. Degli-Alessandrini, J. Bowen, M. Anand, A. Cowley, The microstructure and mechanical properties of microwave-heated lunar simulants at different input powers under vacuum, Sci. Rep. 13 (1) (2023-01) http://dx.doi.org/10.1038/s41598-023-29030-z.

[32] F. Crameri, Scientific colour maps, Zenodo, 2018, http://dx.doi.org/10.5281/zenodo.5501399.